A novel induced pluripotent stem cell model of schwann cell differentiation reveals *NF2*-related gene regulatory networks of the extracellular matrix

Olivia Lazaro[1,*], Sihong Li[1,2,*], William Carter[1], Oluwamayowa Awosika[1], Sylvia Robertson[1], Brooke E. Hickey[3], Steven P. Angus[3,4,5], Austin House[1], D. Wade Clapp[3,4,7], Abdul S. Qadir[1,#], Travis S. Johnson[1,3,4,6,#], Steven D. Rhodes[3,4,7,8#]

[1]Indiana Bioscience Research Institute

[2]Indiana University School of Public Health

[3]Departmaent of Pediatrics, Herman B Wells Center for Pediatric Research, Indiana University School of Medicine, Indianapolis, IN, USA

[4]Melvin and Bren Simon Comprehensive Cancer Center, Indiana University School of Medicine, Indianapolis, IN USA

[5]Department of Pharmacology and Toxicology, Indiana University School of Medicine, Indianapolis, IN, USA

[6]Center for Computational Biology and Bioinformatics

[7]Department of Medical and Molecular Genetics, Indiana University School of Medicine, Indianapolis, IN, USA

[8]Division of Pediatric Hematology/Oncology/Stem Cell Transplant, Indiana University School of Medicine, Indianapolis, IN, USA

[#]**Corresponding authors:** Abdul S. Syed (asyed@indianabiosciences.org), Travis S. Johnson (tjohnson@indianabiosciencs.org), Steven D. Rhodes (sdrhodes@iupui.edu)

Abstract: Schwann cells are vital to development and maintenance of the peripheral nervous system and their dysfunction has been implicated in a range of neurological and neoplastic disorders, including *NF2*-related schwannomatosis. We have developed a novel human induced pluripotent stem cell (hiPSC) model for the study of Schwann cell differentiation in health and disease. We performed transcriptomic, immunofluorescence, and morphological analysis of hiPSC derived Schwann cell precursors (SPCs) and terminally differentiated Schwann-like cells (SLCs) representing distinct stages of development. To further validate our findings, we performed integrated, cross-species analyses across multiple external datasets at bulk and single cell resolution. Our hiPSC model of Schwann cell development shared overlapping gene expression signatures with human amniotic mesenchymal stem cell (hAMSCs) derived SLCs and *in vivo* mouse models, but also revealed unique features that may reflect species-specific aspects of Schwann cell biology. Moreover, we have identified gene co-expression modules that are dynamically regulated during hiPSC to SLC differentiation associated with ear and neural development, cell fate determination, the *NF2* gene, and extracellular matrix (ECM) organization. By cross-referencing results between multiple datasets and analyses, we have identified potential new genes that are related to *NF2* for further study including: *ANXA1, CDH6, COL1A1, COL8A1, MFAP5, IGFBP5, FGF1, AHNAK, CDKN2B, LOX, CAV1*, and *CAV2*. Our hiPSC model further provides a tractable platform for studying Schwann cell development in the context of human disease.

Keywords: Schwann cells, NF2, Schwannoma, hiPSC, RNA-seq, scRNA-seq, gene co-expression analysis, systems biology, extracellular matrix

INTRODUCTION

Schwann cells are glial cells that originate in the neural crest and play a crucial role in myelinating peripheral nerves [1]. Myelination enhances the speed and efficiency of nerve conduction by forming a single spiraling myelin sheath around an axon [2]. Non-myelinating Schwann cells also provide unmyelinated axons with trophic support and mechanical cushioning [3]. Deregulated Schwann cell development can give rise to tumors of the peripheral and cranial nerves called schwannomas [4]. Schwannomas have unpredictable clinical behavior, significant morbidities, and exceedingly limited therapeutic options available for their treatment [5].

Schwannoma development is often associated with an autosomal dominant, heritable genetic condition called *NF2*-related schwannomatosis (*NF2*-SWN, formally known as neurofibromatosis type 2) [6], which is caused by pathogenic variants in the *NF2* tumor suppressor gene, which encodes Merlin, a cytoskeletal adaptor protein with diverse biochemical functions [7]. The development of bilateral vestibular schwannomas is a hallmark of *NF2*-SWN [8]. These tumors involve the eight cranial nerves, which are critical for hearing and balance. Affected individuals often suffer significant morbidities including tinnitus, sensorineural hearing loss, and impairment of balance and coordination [6]. Most vestibular schwannomas occur unilaterally; however, approximately 10% of cases involve both sides and are frequently associated with *NF2*-SWN [9].

To better understand the molecular mechanisms underlying schwannoma genesis in *NF2*-SWN, the development of new model systems for normal and diseased Schwann cells is imperative. Human induced pluripotent stem cells (hiPSCs) have demonstrated promise in modeling a multitude of neurological diseases and cell types, including but not limited to hiPSC-derived astrocytes [10-13], microglia [14-16], and neurons [17, 18]. Direct conversion of human fibroblasts to hiPSC-deviled neurons has also been achieved [18]. These iPSC-derived cells

have been employed to interrogate neuropsychiatric diseases [19-21], neurodegenerative diseases [14, 21, 22], and gliomas [23-25]. However, beyond gliomas, considerably less progress has been made in the field of iPSC modeling of peripheral nervous system derived tumors including schwannoma [26]. Additionally, no hiPSC Schwann cell models derived directly from human fibroblasts have been developed, representing a critical gap in the available model systems for *NF2*-SNW research.

To address this unmet need, we have developed a novel hiPSC Schwann cell model that can be used to study Schwann cell differentiation in health and disease. Here, we performed transcriptomic profiling of hiPSCs at multiple stages of Schwann cell differentiation to unveil broad networks of differentially expressed genes (DEGs) associated with Schwann cell lineage maturation and compare them to the stages outlined by other studies (**Table 1**). To further characterize complex gene regulatory networks (GRNs) associated with Schwann cell differentiation, we employed a systems biology approach, utilizing weighted gene co-expression network analysis (WGCNA) to identify modules of transcriptionally associated genes [27] and to study their temporal dynamics in unison. We further refine the putative roles of these modules using functional enrichment analysis [28]. To validate our findings, we compared the DEGs and gene modules derived from our hiPSC induced Schwann cells with two independent single cell and bulk transcriptomic datasets of human Schwann cell differentiation [29] and mouse sciatic nerve development [30].

METHODS

hiPSC generation

hiPSC lines were generated from neonatal human dermal fibroblasts (HDFn) from Invitrogen (Catalog #: C-004-5C) using an Epi5™ Episomal iPSC Reprogramming Kit (ThermoFisher Scientific) according to manufacturer's protocol. Transduced cells were plated on growth factor

reduced Matrigel (Corning, 356231) coated culture dishes in the presence of ROCK inhibitor and maintained in Essential 8 (E8) medium. iPSC colonies were mechanically isolated and expanded until at least passage 12 before differentiation. iPSCs were characterized by staining with pluripotency markers and embryoid body (EB) formation. Mycoplasma testing was performed prior to Schwann cell differentiation.

Schwann cell differentiation from hiPSCs

The human iPSC line IBRI.101.J was differentiated into Schwann cells using a six-stage protocol over 31 days as described previously [31]. The stages were as follows: stage 1 (day 0 to 3), stage 2 (day 3 to 6), stage 3 (day 6 to 12), stage 4 (day 12 to 18), stage 5 (day 18 to 24), and stage 6 (day 24 to 31). hiPSCs (IBRi 101.J) were seeded on day 0 in a Matrigel plate and fed with S1 media (SCB1 media (NDM containing 1x N2, 1x B27, 0.005% BSA, 2 mM GlutaMAX, 0.11 mM b-mercaptoethanol in advanced DMEM/F12 and Neurobasal medium (1:1 mix)) with CHIR and SB431542) for 6 days. On day 7, cells were fed with S2 media (SCB1 media with CHIR, SB431542 and NRG1) through day 25. On day 26, media was switched to S3 media (SCB2 media (SCDM, DMEM, NEAA, BME, FBS (2%)) with NRG1, Forskolin and PDGF-BB) for 3 days, then to S4 media (SCB2 media with NRG1 and PDGF-BB) for 2 days, and finally to S5 media (SCB2 media with NRG1). By day 31, terminal differentiation to Schwann-like cells was completed. Samples were collected at timepoints aligned with the protocol stages (days: 0, 3, 6, 12, 18, 24, 31) at a uniform 70% confluency in all cases. Cell pellets were collected, and flash frozen at -80°C from three wells for subsequent RNA extraction and RNA-seq, while one well was retained for continued passaging to the next stage.

RNA extraction, library preparation and sequencing

RNA samples were shipped overnight on dry ice to Novogene for quality control, library preparation and RNA-sequencing as further described below. A total of 21 samples, 3 replicates

for each of the 7 timepoints, were sent to Novogene for RNA-sequencing (RNA-seq). CASAVA (Consensus Assessment of Sequence And Variation) base recognition software through the Illumina Genome Analyzer.

Immunoflourescence (IF) staining of hiPSC-derived Schwann cell precursors (SCPs) and Schwann-like cells (SLCs)

We used immunofluorescence (IF) analysis to characterize hiPSC differentiation to SCPs and SLCs [32]. For immunostaining, cells were fixed with 4% Paraformaldehyde for 10 min, permeabilized in 0.1% Triton X-100 (Sigma) for 10 min and blocked in 2% Bovine Serum Albumin (Life Technologies) for 1 hr at room temperature. Cells were then incubated with primary antibodies at 4 °C overnight, then with secondary antibodies for 1 hr at room temperature. The coverslips were mounted on slides with DAPI to stain the nuclei (VectorLabs). Images were captured with an LSM 780 confocal microscope running Zen Black software. Immunocytochemistry analysis confirmed the expression of the Schwann cell markers including S100β, p75, HOXb7, and GAP43.

Initial processing of RNA-sequencing data

Raw reads were removed if they contained adapter sequences, greater than 10% undetermined bases, or more than 50% low-quality bases (quality scores less than 5). Sequenced reads were then aligned to the GRCh38 Genome using HISAT2 v2.0.5 and quantified with feature counts v1.5.0-p3. FPKM values were calculated from the read counts and CDS lengths for each gene across all timepoints and replicates.

Data Cleaning and Quality Control

Statistical analysis was performed using R (v4.1.1.). Genes with the lowest 10% mean FPKM across all timepoints were removed. Ensembl IDs for the filtered genes were converted to HGNC gene symbols using biomaRt (v2.52.0) and the Ensembl gene IDs from the Genome assembly GRCh38.p14 and NCBI RefSeq for annotation. The highest average FPKM Ensembl ID was used for HGNC symbols with multiple corresponding Ensembl IDs.

Differential Gene Expression analysis

Differential gene expression analysis was performed with edgeR v3.22.5. The $\log_2$ fold change (Log_2FC) was calculated between groups and the p-values (P) were corrected using the Benjamini-Hochberg method (BH) to account for the false discovery rate (FDR). Each timepoint (day 3, 6, 12, 18, 24, 31) was compared to baseline (day 0), resulting in 6 pairwise comparisons. DEGs with $Log_2FC > 5.0$ and $FDR < 0.001$ were identified for each comparison. Functional enrichment analysis was performed on DEGs from each comparison using clusterProfiler v3.8.1 to test the statistical enrichment for genes within the Reactome, DO (Disease Ontology), and DisGeNET pathways. Terms with $FDR < 0.05$ were considered enriched. Functional enrichment on other gene sets derived from this analysis was performed using ToppGene [33].

Network Construction and Module Detection with WGCNA and lmQCM

Genes with a maximum expression below the median across all samples were removed to significantly reduce the number of uninformative genes that may bias the analysis. WGCNA module generation was conducted with an unsigned Pearson correlation coefficient (PCC) matrix. Soft thresholding power was calculated to reduce noise for gene correlations and emphasize correlations between genes per WGCNA documentation. A block size of 22000 was used for network construction and module detection as described previously [27]. Eigengenes were subsequently calculated for each module detected by WGCNA. Gene modules whose

eigengene values changed significantly ($P<0.05$) for at least one timepoint were identified by ANOVA. Enrichment analysis was performed using clusterProfiler to identify significantly associated ontology terms for each module. All ontologies inherent to clusterProfiler were evaluated, including BP (biological process), CC (cellular component), and MF (molecular function).

Evaluating Schwann cell differentiation from amniotic mesenchymal stem cells via single cell RNA sequencing

Single cell RNA-seq (scRNA-seq) data from human amniotic mesenchymal stem cells (hAMSCs) differentiated to Schwann like cells (SLCs) was downloaded from Gene Expression Omnibus (GSE161066) [29]. The Seurat R package [34] was used for initial data cleaning and quality control, removing cells with < than 200 or > 2,500 unique feature counts as well as cells with > 5 percent mitochondrial RNAs. The hAMSC and SLCs samples were each normalized with SCTransform [35, 36] and then integrated with Harmony [37, 38]. Uniform manifold approximation and projection (UMAP) [39] was used as a final dimensionality reduction step. The integrated object was clustered, markers were identified for each cluster ($|Log_2FC| > 0.58$ and $FDR<0.05$), and the relative cluster proportions were compared between hAMSCs and SLCs. DGE analysis was also performed between hAMSC and SLCs to identify DEGs specific to either group ($|Log_2FC|>0.58$ and $FDR<0.05$).

Evaluation of Schwann cell differentiation in mouse sciatic nerve

The Sciatic Nerve Atlas (SNAT) RNA-seq dataset FPKM values were downloaded from the SNAT data portal [30]. For gene names with more than one ID, the ID was selected with the highest average expression across all cells in the dataset. Genes with a TPM value > the median TPM value of all genes were retained for downstream analysis. Next, differential gene expression analysis was performed using the edgeR (3.34.1) package. Six comparisons were

performed, one for each timepoint (E17.5, P1, P5, P14, P24, P60) compared to E13.5 as the reference timepoint. Genes were considered differentially expressed if they had a $|Log_2FC| > 5$ and a FDR < 0.001. Genes were mapped to their appropriate human homolog using biomaRt (2.48.3) and the Dec 2021 Ensembl archive for both human and mouse.

Evaluation of myelinating compared to non-myelinating mouse Schwann cells

The SNAT myelination RNA-seq dataset FPKM values were downloaded from the SNAT data portal [30]. The initial processing and homolog mapping steps were as described above. DEGs were compared between myelinating and non-myelinating Schwann cells. Genes were considered differentially expressed if they had a $|Log_2FC| > 5$ and a FDR < 0.001.

Cellular subtyping of Schwann cells from mouse sciatic nerve

The integrated Seurat (4.3.0) object from the SNAT data portal (SS2_all) was downloaded [30] for analysis and comparison with additional datasets. UMAP was calculated on the integrated components using the first 10 dimensions. Marker genes were identified using the FindAllMarkers function. The homolog mapping steps were as previously described. In addition to identifying markers from the previously defined clusters, we also determined DEGs for various differentiation trajectories. Specifically, we identified DEGs using the FindMarkers function contrasting immature Schwann cells (iSCs) from myelinating Schwann cells (mSCs), i.e., iSC vs. tSC and nm(R)SC, and DEGs contrasting iSCs from non-myelinating Schwann cells (nmSCs), i.e., iSC vs. pmSC, mSC cluster 1, mSC cluster 2, and mSC cluster 3 (**Table 1**). Genes were considered differentialy expressed if they had a $|Log_2FC| > 0.58$ and a FDR < 0.05.

Identification of conserved gene expression programs in differentiating Schwann cells across myelination status and species

To examine the similarity of transcriptional programs between mouse and hiPSCs during Schwann cell differentiation, we compared DEGs from our SLC-IU dataset described above and the SNAT RNA-seq dataset for each of the six time point comparisons. First, we calculated the Jaccard index (JI) for the up-regulated DEGs for each pairwise comparison between the SLC-IU and SNAT datasets (i.e., E17 up-regulated DEGs (SNAT) and Day 3 up-regulated DEGs (SLC-IU) JI, E17 up-regulated DEGs (SNAT) and Day 6 up-regulated DEGs (SLC-IU) JI, etc.) The same process was conducted for the down-regulated DEGs, resulting in a total of 36 total JI values for the up-regulated and downregulated DEGs, respectively. We then averaged and normalized the JI values to obtain a square matrix with row and column sums of 1 to account for any skew toward either end of the differentiation process. We then repeated this process with less stringent DEG calling criteria ($|Log_2FC| > 0.58$ and FDR < 0.05). The consistency of the JI matrix was evaluated using a Student's t-test of the diagonal of the matrix vs. the off-diagonal and a Spearman correlation of the JI with the distance of each cell from the diagonal. Next, we compared the union of up-regulated and down-regulated DEGs from both the SLC-IU and SNAT datasets to differentiation and developmental gene modules from the WGCNA analysis using the original criteria ($|Log_2FC| > 5$ and FDR < 0.001). Finally, mSC markers and nmSC markers from the SNAT scRNA-seq dataset were compared to the mSC DEGs identified from the SNAT myelination bulk RNA-seq dataset. We use these comparisons to evaluate the consistency of genes across modalities, species, myelination status, and analysis technique to identify high-confidence targets for the study of Schwann cell differentiation.

RESULTS

Morphological and immunofluorescence-based validation of hiPSC induced differentiation to SPCs and SLCs

To confirm successful differentiation of hiPSCs into Schwann cells precursors (SCPs) and subsequently Schwann like cells (SLCs), we performed morphological and immunofluorescence (IF) staining of cells collected at seven timepoints along the hiPSC to SLC continuum (**Fig. 1**, **Table 2**). We observed morphological changes during the differentiation of hiPSC to SCPs and SLCs where the cells exhibited increasing levels of spatial organization as they became more differentiated (**Fig. 1**). Schwann cells are derived from the neural crest and characterized by the expression of distinct makers including S100β, p75, HOXb7, and GAP43 (**Fig. 2**). A gradual increase in the expression of S100β, p75, HOXb7, and GAP43 was observed throughout the differentiation process reaching a maximum at the SLC stage. Collectively, these findings indicate that our methodology can efficiently generate SCPs and SLPs from hiPSC with high fidelity.

Differential gene expression during SLC differentiation

To characterize dynamic gene expression changes during Schwann cell differentiation, we performed RNA sequencing of cells collected at seven discrete stages along the hiPSC to SLC continuum. As anticipated, replicates from each stage of differentiation clustered together in PCA space (**Fig. 3A**). Notably, the hiPSC stage had clear separation from all other stages (**Fig. 3A**) and the neural rosette (NR) through SCP stages of differentiation clustered more closely together compared to other stages (**Fig. 3A**). There were considerable transcriptional differences between all stages of differentiation, most notably hiPSCs vs later stages of differentiation (**Fig. 4B, Fig S1-S3**). We identified 18 DEGs that were significantly up-regulated DEGs in all 6 comparisons (**Table S1**). Of these, *ANXA1* and *CDH6* were among the top 5 most significant up-regulated DEGs (lowest FDR adjusted p-values) in any of the timepoint comparisons (**Table 3**). Notably, CDH6 is associated with cell-cell adhesion and ANXA1 has been implicated in Schwann cell proliferation and migration [47]. Of the 30 total top 5 up-regulated DEGs per timepoint comparison, 18 were unique across all timepoints. These 18

genes were enriched for ontology terms related to cell adhesion (GO:0007155, *P<0.001*) and anatomical structure formation involved in morphogenesis (GO:0048646, *P<0.001*). In total, 50 significantly down-regulated DEGs were identified at each timepoint comparison (**Table S1**). Anong these, only *AC009446.1, B3GNT7, LINC00678*, and *TDGF1* were also found in the top 5 most significant down-regulated DEGs (lowest FDR adjusted p-values) at any of the timepoint comparisons (**Table 4**). Of the top 5 down-regulated DEGs per timepoint comparison, 18 genes were unique across all timepoints and were enriched for ontology terms related to the regulation of cell fate specification (GO:0042659, *P<0.001*) containing the DEGs *SFRP2, NANOG*, and *DUSP6*.

Gene co-expression modules associated with differentiation, axon guidance and ECM

Building on the results of our differential gene expression analysis, we next performed weighted gene–co-expression network analysis (WGCNA) to identify co-regulated gene modules during hiPSC differentiation to SLCs. WGCNA identified 24 modules (**Fig. S4, File S1**), and 11 of these had significantly altered eigengene values during differentiation (i.e., *P<0.05*, **Table 4**). Of the 11 differentiation-associated modules, 7 had significantly enriched ontology terms associated with them (**Table 4**). The most significant module identified by ANOVA was the brown module (*P<0.001*, **Table 4**, **Fig. 1A**) which had an eigengene peak at day 6, i.e., a significant increase from day 3 to day 6 (*P<0.001*, **Fig. 4A**) followed by a decrease from day 6 to day 12 (*P<0.001*, **Fig. 4A**). Given the close relationship between Schwann cell development and neurons, we were intrigued that the brown module was functionally enriched for axon guidance (P<0.001, **Fig. 4B**, **File S2**), forebrain development (*P<0.001*, **Fig. 4B**, **File S2**), and sensory organ morphogenesis (*P<0.001*, **Fig. 4B**, **File S2**).

The next two most significant modules were red (P<0.001) and turquoise (P<0.001) (**Table 4**). The red module eigengene steadily increased from the hiPSC to SCP stage (*P<0.001*, i.e., day

0 to day 24, **Fig. S5**) then dramatically decreased from the SCP to SLC stage (*P<0.001*, i.e., day 24 to day 31, **Fig. S5**) and was functionally enriched for biosynthetic pathways (**Fig. S5**, **File S3**). In contrast, the turquoise module eigengene, which was functionally enriched for functionally enriched for exocytosis (*P<0.001*, **Fig. S6**, **File S4**) and regulation of neuron project development (*P<0.001*, **Fig. S6**, **File S4**) decreased dramatically from the hiPSC to preneural rosette (pre-NR) stage (*P<0.001*, i.e., day 0 to day 3, **Fig. S6**) and remained suppressed through terminal SLC differentiation (*P=0.732*, i.e., day 3 to day 31, **Fig. S6**). Another pair of modules that showed distinct expression patterns were the pink and blue modules (*P<0.001* and *P<0.001* respectively, **Table 4**). Similar to the brown module that had a distinct eigengene peak at day 6, the pink module peaked at day 12, i.e., a significant increase from day 6 to day 12 (*P<0.001*, **Fig. 4C**) and decreased thereafter from day 12 to day 18 (*P<0.001*, **Fig. 4C**). Not surprisingly, this module had numerous ontology terms related to cell fate commitment and ear development (**Fig. 4D, File S6**). The blue module eigengene also had a peak early in hiPSC to SLC differentiation at day 3, i.e., a significant increase from day 0 to day 3 (*P<0.001*, **Fig. 4E**) and decrease from day 3 to day 6 (*P<0.001*, **Fig. 4E**). However, this module eigengene gradually increased again from NR through completion of SLC maturation (*P<0.001*, **Fig. 4E**). Notably, the blue module contains the *NF2* tumor suppressor gene and had significant functional enrichment for extracellular matrix organization (*P<0.001*, **Fig. 4F**, **File S7**), extracellular structure organization (P<0.001, **Fig. 4F**, **File S7**), and cell-substrate adhesion (*P<0.001*, **Fig. 4F**, **File S7**). Taken together with the remaining modules (**Fig S7-S12**, **File S5, S8-S12**), the results of our WGCNA reveal that hiPSC differentiation to SLCs is associated with dynamic changes in gene expression that are reflective of Schwann cell biological function and show clear associations with neural morphology, ear development, and cellular organization.

Signatures of hAMSC to SLC differentiation are unique at the single cell level

To evaluate the robustness and generalizability of our findings, we extended our analysis to examine whether similar gene modules and pathways were retained in other complementary models of human Schwann cell differentiation. Wei and colleagues performed single cell RNA-sequencing of Schwann cell like cells (SLCs) derived from human amniotic mesenchymal stem cells (hAMSCs) to identify heterogenous SLCs populations [29] (GSE161066). The scRNA-seq data contained 3,892 hAMSCs and 1,729 SLCs. After quality control (QC) and dimensionality reduction, we identified a total of 16 clusters (**Table 2**, **Fig. 5A**). DGE analysis revealed clear differences between hAMSC and SLCs. Some of the most upregulated genes in SLCs included ISG*15*, *IFI27*, *COL3A1*, and *IFI6*, while the most highly expressed genes in hAMSCs included *EEF1A1* and *TPT1*, (**Fig. 5B**, **Table 5**). To further characterize each cluster, we performed cluster-specific marker analysis using Seurat to identify distinct gene sets highly expressed in each cluster (**Fig. 5C**). We observed that some clusters had a higher proportion of either hAMSCs or SLCs, suggesting that they may represent different stages of differentiation **(Fig. 5D**). For example, cluster 4, 8, and 14 were comprised of a higher proportion of SLCs, whereas clusters 5, 10, and 13 were characterized by a relative abundance of hAMSCs (**Fig. 5D**). The markers for these hAMSC-related clusters included: cluster 4 (*TAGLN*, *TPM1*, and *TPM2*), cluster 8 (*TUBA1B*, *H2AFZ*, and *VIM*), cluster 10 (*IGFBP7*, *CXCL8*, *B2M)*, and cluster 14 (*MEG3*, *NEAT1*, *VMP1*, *MALAT1*, *CALD1*, and *TPM1*) (**Fig. 5C**, **Table 6**, **Table S1**).Interestingly, *TPM1* has been reported as a tumor suppressor in renal cell carcinoma [40, 41].

Evaluation of Schwann cell differentiation in mouse sciatic nerve

To further validate our hiPSC model of Schwann cell differentiation *in vitro*, we further compared our transcriptomic data with an *in vivo* dataset comprehensively cataloging Schwann cell development in the mouse sciatic nerve. Gerber and colleagues generated gene expression profiles from Schwann cells isolated from mouse sciatic nerve throughout embryogenesis and

postnatal development, which are publicly available through the Sciatic Nerve Atlas (SNAT). By integrating bulk and single cell RNA-seq data from SNAT, we identified unique and conserved gene signatures of Schwann cell differentiation across species and modalities.

In our SLC-IU dataset, a total of 50 genes were significantly up-regulated across all timepoints (**Table S2**). These genes represented myelination (GO:0042552, *P<0.001*) and collagen-containing extracellular matrix (GO:0062023, *P<0.001*). In contrast to the SLC-IU dataset, which had more down-regulated DEGs at all six timepoints than up-regulated DEGs at all six timepoints, in this dataset (SNAT), there were 362 down-regulated DEGs representing seven times as many as up-regulated DEGs (**Fig. 6A-F, Table 7**). The 362 down-regulated DEGs significant at all comparisons were enriched for neuron development (GO:0048666, *P<0.001*) and synaptic signaling (GO:0099536, P<0.001). Furthermore, we identified 9 gene coexpression modules that were significantly altered over developmental stage from E13 to P60.(**Table S3**, **File S13**). Notably some of these modules were also enriched for terms related to neural development like the SNAT-brown module (GO:0010975, Regulation of neuron projection development, *P<0.001*, **Table S2, File S14-S22**).

Differential gene expression and enrichment in myelinating versus non-myelinating murine Schwann cells

We next sought to investigate the gene expression profiles of myelinating (mSCs) and non-myelinating (nmSCs) in the Sciatic Nerve Atlas. mSCs had 478 up-regulated DEGs and 471 down-regulated DEGs in comparison to nmSCs (**Fig. 6G, Table 8**). These up-regulated DEGs were enriched for structural constituents of myelin sheath (GO:0019911, *P=0.039*), myelination (GO:0042552, *P<0.001*), and sterol biosynthetic processes (GO:0016126, *P<0.001*). Down-regulated DEGs were highly enriched for mitotic cell cycle (GO:0000278, *P<0.001*), cell division

(GO:0051301, *P<0.001),* and positive regulation of cell cycle processes (GO:0090068, *P<0.001*).

Myelinating and non-myelinating Schwann cell subsets remained largely distinct even upon recomputing the UMAP dimensionality reduction (**Fig. 7A**)[31]. Two distinct trajectories emerged, beginning from proliferating Schwann cells (prol. SC) and terminating at either mSC cluster 3 or nm(R)SC (**Fig. 7A**)[31]. We observed 261 up-regulated and 116 down-regulated DEGs in myelinating Schwann cells (mSC) as compared to immature Schwann cells (iSCs) (**Table 9**). As expected, the up-regulated DEGs in mSCs were enriched for terms related to regulation of nervous system development (GO:0051960, P<0.001) and myelination (GO:0042552, P<0.001). However, the most significantly enriched term was sterol biosynthetic process (GO:0016126, P<0.001). The robust upregulation of cell cycle inhibitors including *CDKN1A* (**Fig. 7B**) in conjunction with the downregulation of cyclins such as *CDK6* (**Fig. 7B**) a state of growth arrest in this cluster. In non-myelinating Schwann cells (nmSCs), we identified 108 up-regulated and 67 down-regulated DEGs in comparison to iSCs (**Table 9**). The up-regulated DEGs in nmSCs were enriched for terms related to complement activation (GO:0006956, P=0.002), gliogenesis (GO:0042063, P=0.002), positive regulation of programmed cell death (GO:0043068, P=0.006), and negative regulation of developmental process (GO:0051093, P=0.007). Notably, complement cascade members including *C4A, SERPING1* (**Fig. 7C**), *CLU, RGCC, CD59*, and *C1R* were upregulated. Furthermore, *C4A* and *SERPING1* had the two highest positive fold changes of all genes tested highlighting an association between the complement cascade and nmSCs. Using as few as three transcriptomic markers, we could distinguish the stages of Schwann cell differentiation and the bifurcation of mSCs and nmSC (**Fig. 7D, Table 10**).

Differentiating Schwann cells have conserved pathways related to extracellular matrix

As anticiatped, the transcriptional signatures of Schwann cells differentiation were not idneticaly conserved between hiPSCs and mice, likely due to both species and model specific differences (*in vitro* vs *in vivo*). Both the up-regulated and down-regulated DEG Jaccard indices (JIs) showed low Pearson correlation coefficients (PCCs) and were statistically insignificant (**Fig. 8A-DB**, *P=0.308* and *P=0.535*, respectively) using stringent DEG criteria ($|Log_2FC| > 5$ and an FDR < 0.001). Even when the JIs were were averaged and normalized, their association remain insignificant (**Fig. 8E-F**, *P=0.674*). However, with less stringent criteria ($|Log_2FC| > 0.58$ and an FDR < 0.05), a moderate association emerged (**Fig. 8G-H**, *P=0.0843*).

We focused on the blue module and turquoise module and compared them to the up- and down-regulated DEGs from the SLC-IU and SNAT datasets. The blue module contained *NF2* and the eigengene trended upward throughout the differentiation process, whereas the turquoise module trended downward. The up-regulated DEGs from both SLC-IU and SNAT had high overlap with the blue module, but low overlap with one another (**Fig. 8I**). In contrast the SLC-IU up-regulated DEGs had lower overlap with the turquoise module, while SNAT up-regulated DEGs had a similar number of DEGs in the turquoise module (**Fig. 8J**). Both the SLC-IU and SNAT down-regulated DEGs had lower overlap with the blue module (**Fig. 8K**) than with the turquoise module (**Fig. 8L**). Notably 21 genes representing specific molecular functions including extracellular matrix structural constituent (GO:0005201, P=0.005) and S100 protein binding (GO:0044548, P=0.008) and biological processes including caveola assembly (GO:0070836, P=0.006) and regulation of transforming growth factor beta receptor signaling pathway (GO:0017015, P=0.006), were contained within the blue module(**Table S2**) and were upregulated in both the SLC-IU and SNAT datasets.

In addition to these unique conserved processes during mouse and hiPSC Schwann cell differentiation, mSCs had distinct molecular profiles in comparison to nmSCs that were recapitulated in both RNA-seq and scRNA-seq data modalities. Notably, mSC up-regulated

DEGs from SNAT RNA-seq exhibited a high degree of overlap with mSC markers from the SNAT scRNA-seq dataset (**Fig. 8M**). Interestingly there were eight genes that also overlapped with the nmSC markers namely: *CNTF, OGN, CFAP100, ZFP91, CCDC152, SELENOP, GPR37L1*, and *IL34*. Similarly, nmSC down-regulated DEGs from SNAT RNA-seq have high overlap with nmSC markers form SNAT scRNA-seq (**Fig. 8N**). Interestingly, there were still 12 markers also overlapping with iSC markers namely: *CCND1, HDAC4, RBP1, EPHA5, DAB1, EDNRB, ALCAM, NAV2, POSTN, DAB2, EGR3*, and *SMIM5*.

DISCUSSION

We have developed a platform to study Schwann cell development using hiPSCs. We demonstrate that hiPSCs successfully differentiated into SLCs based on marker gene expression and morphology. Furthermore, we identify similar transcriptomic profiles in our hiPSC to SLC differentiation model as observed in other external Schwann cell differentiation studies [29, 30]. Notably, we observed correlation of DEGs and gene expression signatures including…. between hiPSC derived SLCs and SCs from the developing mouse sciatic nerve [30]. However, key differences between our hiPSC model and the mouse Schwann cell development also emerged, which may be attributable to both species-specific differences as well as the model system employed (*in vitro* versus *in vivo*). Transcriptional discordance between SLCs derived from hAMSCs versus hiPSCs may in part be attributable to unique cells of origin and the experimental differences related to the reprograming process. While hiPSCs have been utilize successfully to overcome limitations of mouse models to develop to enhance our understanding of psychiatric disorders [42] and Alzheimer's disease [22], further investigation is needed to the validate the fidelity of this platform in recapitulating the pathogenesis of NF2-SWN and other Schwann cell associated disorders.

Importantly, despite these differences, our analysis did reveal novel gene signatures associated with Schwann cell development that were conserved across species and model systems. We identified gene coexpression modules related to differentiation, notably the blue module that contained the *NF2* tumor suppressor gene. This module was functionally enriched for multiple terms related to extracellular matrix and actin filaments, which is consistent with the relationship between *NF2* and F-actin cytoskeletal defects in schwannoma [43]. Moreover, CAV*1* and *CAV2,* two of the blue module genes conserved in both hiPSC and mouse derived SCs, may be linked to *NF2*-associated vesicle trafficking as previously shown in schwannoma [44]. Growth factors and cell cycle inhibitors, such as *LOX* and *CDKN2B*, were also present in the blue module and conserved in cross-species analysis. *LOX* is a tumor suppressor gene, which when mutated in Schwann cells, can suppress T-cells in the melanoma tumor microenvironment [45]. *CDKN2B* is a cell cycle inhibitor that can induce proliferation when deleted or mutated in a multitude of cancer types [46-48]. Furthermore, we identified hiPSC-specific genes of interest that were highly up-regulated during SLC differentiation and differentially expressed at all timepoints, namely *ANXA1* and *CDH6*. CDH6 (Cadherin-6) encodes a member of the cadherin superfamily and mediates homophilic cell-cell adhesion, yet its relationship to Merlin in Schwann cell biology remains understudied. Finally, ANXA1 has been implicated in promoting Schwann cell proliferation and migration and represents another promising target for future investigation[49].

In summary, we developed a novel hiPSC Schwann cell differentiation model and performed integrated analyses across five datasets from three independent studies, including both scRNA-seq and RNA-seq. We demonstrate that our hiPSC model robustly recapitulates Schwann cell development and identifies novel Schwann cell differentiation genes for further study. Future studies leveraging this platform to conduct CRISPR-Cas9 editing of *NF2* and other associated genes relevant to SC differentiation/function, generate hiPSC organoid co-cultures, and perform

bulk and single cell mulitomics analysis will reveal new insights into Schwann cell biology and Schwannoma genesis in *NF2*-SWN.

ACKNOWLEDGEMENTS

We would like to acknowledge the help and support of the Indiana University School of Medicine Center of Computational Biology and Bioinformatics, the Indiana University Information Technology Services for their high-performance computing resources, and the Indiana Biosciences Research Institute for their lab and technical support.

FUNDING

Funding from the Indiana Biosciences Research Institute to A.S. and T.S.J., 1R21CA264339 to T.S.J., S.D.R. is supported by the Francis S. Collins Scholars Program in Neurofibromatosis Clinical and Translational Research funded by the Neurofibromatosis Therapeutic Acceleration Program (NTAP, 2004757180), a K08 Mentored Clinical Scientist Research Career Development Award funded by the NIH/National Institute of Neurological Disorders and Stroke (NINDS) (K08-NS128266-02), and startup funding from the Department of Pediatrics at the Indiana University (IU) School of Medicine and the IU Simon Comprehensive Cancer Center (IUSCCC).

DISCLOSURES

O.L., W.C., A.H., A.Q., T.S.J., are partially supported by the Indiana Biosciences Research Institute. A.H. currently holds a research position at Eli Lilly and Company.

AUTHOR CONTRIBUTIONS

S.D.R, A.S.Q, and T.J. designed the experiments and evaluated the data. W.C, A.H, A.S.Q, and B.E.H. performed the experiments. O.L, S.L, and T.J analyzed all data and prepared the graph. T.J, S.L, A.S.Q, and S.D.R wrote the initial draft of the manuscript. S.P.A and D.W.C. gave advice during the project achievement. All co-authors provided feedback and revisions.

TABLES

Table 1. Abbreviations for Schwann cells, precursors, and iPSC derived cells.

hiPSC	Human induced pluripotent stem cells
SC	Schwann cells
SLC	Schwann-like cells
SPC	Schwann cell precursors
iSC	Immature SCs
mSC	Myelinating SCs
tSC	Transition SCs
pmSC	Pro-myelinating SCs
nmSC	Not-myelinating SCs
nm(R)SC	Non-myelinating (Remak) SCs

Table 2. Table of the datasets used for analysis in this study

Dataset name	Samples	Description	Publication	PMID	Accession
SLC-IU	21 samples RNA-seq (3 replicates across 7 timepoints) RNA-seq	hiPSC to SLC differentiation sampled at seven timepoints Organism: Human	This study	This study	This study
SLC-SUMC	2 samples (1 hAMSC sample with 3,892 cells and 1 SLC sample with 1,729 cells) scRNA-seq	hAMSC to SLC differentiation sampled at hAMSC and SLC stages Organism: Human	Wei, Z. frontiers in Physiology. (2021)	34093220	GSE161066
SNAT	28 samples (4 replicates across 7 timepoints) RNA-seq; 8 FACS samples (4 mSC and 4 nmSC) RNA-seq; 8 samples (2 replicates across 4 stages: P1, P5, P14, and P60) scRNA-seq	SCP to SC differentiation; Comparison of mSC and nmSCs; Cellular subtyping of Schwann cells during stages of development. Organism: Mouse	Gerber, D. eLife. (2021)	33890853	GSE137870

Table 3. Top 5 up- and down-regulated DEGs for each of the 6 timepoints (k) compared to day 0.

Day k vs. Day 0	Gene	Log2FC	P	FDR
Day 3 Up	COL8A1	11.33	0	0
Day 3 Up	POSTN	10.15	0	0
Day 3 Up	SERPINE1	9.22	0	0
Day 3 Up	IGFBP3	7.61	0	0
Day 3 Up	TGFBI	7.15	0	0
Day 3 Down	CD24	-6.37	5.14E-260	8.69E-257
Day 3 Down	EPCAM	-7.93	1.19E-229	1.07E-226
Day 3 Down	HLA-A	-5.53	5.65E-213	4.16E-210
Day 3 Down	PMEL	-7.55	7.08E-213	5.08E-210
Day 3 Down	ESRG	-9.76	7.22E-212	5.06E-209
Day 6 Up	HAPLN1	6.97	8.78E-236	2.53E-231
Day 6 Up	CDH6	5.91	1.68E-227	2.43E-223
Day 6 Up	PRTG	4.91	4.72E-225	4.54E-221
Day 6 Up	WLS	5.36	1.57E-184	7.55E-181
Day 6 Up	GREB1L	6.90	2.12E-183	8.73E-180
Day 6 Down	TDGF1	-5.01	8.98E-198	6.47E-194
Day 6 Down	ADCY2	-6.77	1.89E-190	1.09E-186
Day 6 Down	LINC00678	-5.15	2.72E-151	7.83E-148
Day 6 Down	AC064802.1	-4.65	9.03E-148	2.37E-144
Day 6 Down	DUSP6	-4.65	7.95E-145	1.64E-141
Day 12 Up	ANXA1	10.95	4.31E-276	6.09E-272
Day 12 Up	CPE	5.72	2.35E-191	1.67E-187
Day 12 Up	PLK2	5.42	1.95E-190	1.11E-186
Day 12 Up	PRTG	4.52	1.72E-185	8.13E-182
Day 12 Up	CDH6	5.53	4.22E-181	1.71E-177
Day 12 Down	TDGF1	-8.16	0	0
Day 12 Down	AC064802.1	-8.52	7.05E-207	6.65E-203
Day 12 Down	NANOG	-7.30	7.96E-173	2.82E-169
Day 12 Down	USP44	-5.13	5.67E-164	1.46E-160
Day 12 Down	AC009446.1	-7.39	2.73E-162	6.42E-159
Day 18 Up	ANXA1	10.79	0	0
Day 18 Up	COL8A1	10.92	0	0
Day 18 Up	CAV1	6.12	0	0
Day 18 Up	SERPINE1	8.14	5.48E-295	3.85E-291
Day 18 Up	POSTN	8.01	2.79E-294	1.56E-290
Day 18 Down	TDGF1	-10.73	2.01E-273	7.06E-270
Day 18 Down	USP44	-5.52	1.62E-253	4.54E-250
Day 18 Down	ZSCAN10	-6.42	3.59E-216	4.03E-213

Day 18 Down	ESRG	-5.16	8.92E-199	7.82E-196
Day 18 Down	VSNL1	-7.28	3.70E-179	2.16E-176
Day 24 Up	ANXA1	11.19	0	0
Day 24 Up	POSTN	8.43	0	0
Day 24 Up	CAV1	6.16	0	0
Day 24 Up	PLK2	5.77	0	0
Day 24 Up	SPP1	4.22	1.63E-291	9.33E-288
Day 24 Down	USP44	-5.49	8.04E-274	2.29E-270
Day 24 Down	ESRG	-5.53	8.55E-249	1.22E-245
Day 24 Down	ZSCAN10	-7.03	1.28E-236	1.52E-233
Day 24 Down	PMEL	-4.70	6.92E-211	6.17E-208
Day 24 Down	B3GNT7	-6.79	7.86E-201	5.98E-198
Day 31 Up	CTGF	6.05	0	0
Day 31 Up	VIM	6.55	0	0
Day 31 Up	COL5A2	7.04	0	0
Day 31 Up	COL8A1	11.75	0	0
Day 31 Up	POSTN	9.95	0	0
Day 31 Down	CD24	-6.94	0	0
Day 31 Down	HLA-A	-6.02	8.07E-296	7.22E-293
Day 31 Down	SFRP2	-5.66	3.19E-289	2.61E-286
Day 31 Down	L1TD1	-5.78	4.22E-275	3.26E-272
Day 31 Down	EPCAM	-7.92	1.74E-267	1.18E-264

Table 4. Significantly altered gene modules in relation to timepoint evaluated by ANOVA. The number of genes in the module, ANOVA P, and most significant GO term are listed for each module. Modules with no significant GO terms are blank.

Module	Genes	P	Top GO term	File
Brown	1449	7.66E-17	Axon guidance	File S2
Red	845	2.63E-14	Organic hydroxy compound biosynthetic process	File S3
Turquoise	4615	5.23E-14	Nuclear chromosome segregation	File S4
Cyan	100	1.38E-11		File S5
Pink	692	2.11E-11	Cell fate commitment	File S6
Blue	3797	2.16E-10	Extracellular matrix organization	File S7
Black	833	1.73E-8	Intraciliary transport particle B	File S8
Magenta	159	4.99E-5	Endoplasmic reticulum protein-containing complex	File S9
Yellow	1288	1.52E-2	Cytoplasmic translation	File S10
Midnight Blue	78	4.19E-2	Transcription coregulator activity	File S11

Green Yellow	146	4.26E-2	Methyltransferase activity	File S12

Table 5. Top 10 up- and down-regulated DEGs in hAMSCs versus SLCs from the SLC-SUMC dataset

Gene	Proportion hAMSCs>0	Proportion SLCs>0	Log_2FC	P	FDR
ISG15	0.04	0.44	0.66	1.00E-300	0.00E+00
IFI27	0.02	0.32	0.61	4.98E-256	5.71E-252
IFI6	0.01	0.27	0.45	1.37E-210	1.58E-206
COL3A1	0.07	0.40	0.55	2.62E-202	3.00E-198
COL1A1	0.06	0.34	0.49	6.85E-174	7.86E-170
LGALS1	0.49	0.81	0.68	2.36E-171	2.71E-167
EEF1A1	0.97	0.88	-0.58	1.66E-158	1.90E-154
BST2	0.02	0.22	0.34	1.86E-139	2.14E-135
TPT1	0.96	0.88	-0.55	1.79E-133	2.05E-129
TPM1	0.31	0.60	0.61	1.85E-118	2.12E-114
TMSB10	0.88	0.95	0.47	2.17E-99	2.49E-95
S100A6	0.47	0.70	0.55	3.15E-99	3.62E-95
RPL3	0.83	0.66	-0.45	8.45E-81	9.70E-77
CXCL8	0.71	0.48	-0.55	9.51E-79	1.09E-74
IGF2	0.20	0.01	-0.34	6.67E-76	7.65E-72
RPS3A	0.80	0.61	-0.42	1.52E-72	1.75E-68
SAT1	0.35	0.12	-0.37	7.64E-72	8.77E-68
MT2A	0.98	0.98	-0.58	1.37E-70	1.57E-66
RPS12	0.89	0.77	-0.40	1.54E-70	1.77E-66
RPS6	0.76	0.57	-0.40	6.27E-67	7.20E-63

Table 6. Significant marker DEGs for the clusters identified from the SLC-SUMC dataset corresponding to rows in **Fig 5C**.

Gene	Cluster	Proportion cluster > 0	Proportion other clusters >0	Log2FC	P	FDR
FTL	2	0.99	0.93	0.68	1.23E-58	1.41E-54
FTH1	2	1.00	0.98	0.60	7.23E-42	8.3E-38

CXCL1	3	0.96	0.79	1.15	1.46E-144	1.68E-140
TIMP1	3	0.89	0.60	1.34	8E-131	9.19E-127
TFPI2	3	0.79	0.47	1.12	2.22E-110	2.54E-106
TAGLN	4	0.90	0.28	1.43	4.22E-242	4.85E-238
TPM1	4	0.80	0.36	1.02	4.94E-122	5.68E-118
TPM2	4	0.92	0.60	1.09	7.95E-121	9.12E-117
RAB13	6	0.87	0.28	1.88	7.64E-144	8.77E-140
IGFBP5	6	0.70	0.34	1.30	8.01E-50	9.19E-46
TAGLN	6	0.48	0.32	0.75	5.37E-10	6.17E-06
MALAT1	7	0.82	0.51	0.68	4.26E-40	4.89E-36
TUBA1B	8	0.68	0.18	0.95	1.5E-88	1.73E-84
H2AFZ	8	0.73	0.27	0.87	2.32E-70	2.66E-66
VIM	8	0.79	0.52	0.74	2.35E-27	2.7E-23
IGFBP7	10	0.44	0.18	0.83	1.71E-17	1.97E-13
CXCL8	10	0.89	0.63	1.36	2.39E-14	2.74E-10
B2M	10	0.61	0.37	0.97	2.28E-13	2.61E-09
NEAT1	12	0.51	0.16	0.72	1.27E-25	1.46E-21
PAPPA	12	0.36	0.11	0.75	5.37E-18	6.17E-14
MALAT1	12	0.70	0.52	0.93	1.11E-09	1.27E-05
NEAT1	14	0.73	0.15	4.25	4.5E-63	5.17E-59
VMP1	14	0.48	0.08	1.60	7.26E-50	8.34E-46
MALAT1	14	0.91	0.52	5.12	6.99E-39	8.02E-35
TSC22D1	15	0.50	0.04	1.69	1.86E-26	2.13E-22
SNHG15	15	0.14	0.01	1.11	2.84E-08	3.26E-04
RHEB	15	0.46	0.12	1.34	8E-07	9.19E-03

Table 7. Top 5 up- and down-regulated DEGs for each of the 6 stages (k) compared to E13 in the SNAT RNA-seq dataset.

Stage k vs. Stage E13	Gene	Log_2FC	P	FDR
E17 Up	MAL	6.84	6.86E-95	1.42E-90
E17 Up	ART3	8.44	2.00E-94	2.08E-90
E17 Up	GJC3	8.22	5.23E-79	2.71E-75
E17 Up	LAMA2	7.16	3.07E-67	7.08E-64

E17 Up	SBSPON	11.07	9.40E-63	1.63E-59
E17 Down	MAPT	-8.30	4.04E-84	2.79E-80
E17 Down	INA	-10.32	2.09E-69	7.24E-66
E17 Down	STMN2	-8.45	2.91E-69	8.62E-66
E17 Down	GAP43	-7.60	2.09E-65	4.34E-62
E17 Down	RTN1	-7.61	1.05E-63	1.98E-60
P1 Up	GJC3	10.96	2.48E-115	5.15E-111
P1 Up	CLDN19	12.85	1.49E-113	1.55E-109
P1 Up	PMP22	8.96	2.36E-110	1.63E-106
P1 Up	PMP2	13.17	2.42E-109	1.26E-105
P1 Up	FABP9	13.15	2.15E-106	8.91E-103
P1 Down	STMN2	-9.90	6.00E-70	6.23E-67
P1 Down	GAP43	-9.27	6.48E-69	6.12E-66
P1 Down	MAPT	-7.39	7.38E-69	6.66E-66
P1 Down	DPYSL3	-6.70	3.11E-62	2.30E-59
P1 Down	CRMP1	-11.78	8.43E-62	5.75E-59
P5 Up	PMP22	11.53	8.87E-209	1.84E-204
P5 Up	MBP	12.53	1.73E-171	1.80E-167
P5 Up	PMP2	15.02	6.84E-158	4.73E-154
P5 Up	CLDN19	13.74	1.44E-152	7.48E-149
P5 Up	FABP9	14.99	7.22E-152	3.00E-148
P5 Down	STMN2	-10.12	1.96E-73	1.23E-70
P5 Down	GAP43	-9.66	1.09E-71	6.44E-69
P5 Down	DPYSL3	-7.07	2.56E-71	1.43E-68
P5 Down	INA	-11.51	4.25E-64	1.88E-61
P5 Down	CRMP1	-13.45	7.73E-61	2.97E-58
P14 Up	PMP22	12.84	1.34E-239	2.77E-235
P14 Up	MBP	13.79	7.41E-187	7.69E-183
P14 Up	MAL	10.44	4.76E-177	3.29E-173
P14 Up	PMP2	15.41	2.11E-169	1.09E-165
P14 Up	FABP9	15.39	1.32E-162	5.49E-159
P14 Down	GAP43	-9.38	2.39E-69	8.56E-67
P14 Down	STMN2	-9.36	5.84E-69	2.04E-66
P14 Down	INA	-13.07	1.19E-63	3.21E-61
P14 Down	BASP1	-10.25	4.51E-63	1.14E-60
P14 Down	DPYSL3	-6.31	1.22E-60	2.85E-58
P24 Up	PMP22	12.93	5.98E-201	1.24E-196
P24 Up	MBP	13.38	3.01E-173	3.12E-169
P24 Up	PMP2	15.66	7.27E-150	5.03E-146

P24 Up	PRX	12.00	2.38E-149	1.24E-145
P24 Up	FABP9	15.63	1.24E-143	5.16E-140
P24 Down	GAP43	-9.38	1.71E-68	6.69E-66
P24 Down	INA	-14.66	5.67E-65	1.93E-62
P24 Down	BASP1	-9.92	4.82E-62	1.49E-59
P24 Down	MEST	-6.56	7.22E-61	2.14E-58
P24 Down	CRMP1	-14.53	3.92E-60	1.13E-57
P60 Up	PMP22	12.03	6.44E-205	1.34E-200
P60 Up	APOD	11.84	9.53E-186	9.89E-182
P60 Up	CNTF	14.44	9.13E-173	6.31E-169
P60 Up	MBP	12.50	1.71E-157	5.93E-154
P60 Up	DRP2	10.64	3.58E-156	1.06E-152
P60 Down	MEST	-10.27	1.21E-98	8.67E-96
P60 Down	INA	-14.05	8.93E-68	2.52E-65
P60 Down	BASP1	-10.80	4.56E-67	1.23E-64
P60 Down	GAP43	-8.43	8.41E-67	2.21E-64
P60 Down	DPYSL3	-6.96	6.41E-64	1.53E-61

Table 8. Top 10 up- and down-regulated DEGs in mSCs versus nmSCs from the SNAT RNA-seq dataset.

Gene	Log_2FC	P	FDR
CAV1	8.18	1.14E-92	1.46E-88
PMP22	5.06	2.99E-88	1.92E-84
MBP	4.48	3.72E-83	1.59E-79
OGN	5.73	8.09E-80	2.59E-76
PMP2	6.57	8.89E-78	2.28E-74
FABP9	6.57	5.10E-75	1.09E-71
KCNK1	6.19	1.64E-72	3.01E-69
HMGCS1	4.67	1.72E-68	2.76E-65
CNTF	8.20	3.32E-63	4.73E-60
HLA-DMB	7.56	1.71E-62	2.19E-59
SPARCL1	-5.50	4.07E-58	3.48E-55
ENTPD2	-6.21	1.17E-55	7.91E-53
EDNRB	-4.13	2.47E-53	1.44E-50
TOP2A	-5.22	2.05E-52	1.10E-49
SMIM5	-6.69	3.69E-52	1.89E-49
POSTN	-5.01	9.13E-52	4.19E-49

NCAM1	-5.16	1.82E-51	8.05E-49
SLC43A3	-6.03	3.43E-51	1.47E-48
S1PR3	-6.36	5.58E-49	2.31E-46
L1CAM	-6.15	1.87E-48	7.27E-46

Table 9. Top 10 up- and down-regulated DEGs in mSC and nMSC compared to iSC in the SNAT scRNAseq dataset.

Cluster vs iSC	Gene	Proportion cluster > 0	Proportion other clusters >0	Log_2FC	P	FDR
mSC Up	NCMAP	0.96	0.18	2.36	3.91E-245	6.14E-241
mSC Up	MPZ	1.00	0.99	0.72	6.62E-227	1.04E-222
mSC Up	EMID1	0.92	0.17	1.96	2.48E-218	3.90E-214
mSC Up	PLLP	1.00	0.65	1.05	3.71E-212	5.83E-208
mSC Up	FXYD6	0.93	0.22	1.84	7.08E-212	1.11E-207
mSC Up	SLC36A2	0.88	0.09	2.06	3.76E-209	5.90E-205
mSC Up	PRX	0.99	0.78	0.81	8.18E-207	1.28E-202
mSC Up	FA2H	0.96	0.27	1.56	2.50E-206	3.92E-202
mSC Up	CLDN19	0.99	0.48	1.24	1.86E-194	2.91E-190
mSC Up	CDKN1A	0.98	0.57	1.11	8.05E-193	1.26E-188
mSC Down	EDNRB	0.87	1.00	-1.19	1.38E-203	2.16E-199
mSC Down	SPARCL1	0.59	0.96	-1.34	5.24E-178	8.22E-174
mSC Down	COL3A1	0.92	1.00	-0.90	8.02E-164	1.26E-159
mSC Down	NCAM1	0.51	0.95	-1.27	1.79E-159	2.80E-155
mSC Down	SOSTDC1	0.94	0.98	-0.70	2.53E-155	3.98E-151
mSC Down	POSTN	0.37	0.85	-1.51	2.66E-153	4.17E-149
mSC Down	MARCKS	0.92	1.00	-0.67	1.18E-150	1.85E-146

mSC Down	CDK6	0.60	0.91	-1.17	4.10E-140	6.44E-136
mSC Down	RARRES2	0.64	0.89	-1.13	1.11E-133	1.74E-129
mSC Down	LRRC61	0.55	0.88	-1.09	1.38E-131	2.17E-127
nmSC Up	PRNP	0.98	0.81	0.69	9.16E-138	1.44E-133
nmSC Up	SCN7A	0.89	0.44	1.15	1.61E-119	2.52E-115
nmSC Up	PRND	0.90	0.61	0.90	1.64E-112	2.57E-108
nmSC Up	SERPING 1	0.75	0.19	1.44	1.90E-112	2.99E-108
nmSC Up	GPR37L1	0.79	0.24	1.31	4.24E-112	6.66E-108
nmSC Up	FXYD1	0.98	0.84	0.64	1.41E-111	2.21E-107
nmSC Up	ENTPD2	0.91	0.59	0.85	3.08E-107	4.84E-103
nmSC Up	HLA-E	0.83	0.32	1.21	5.46E-105	8.58E-101
nmSC Up	CPE	0.96	0.66	0.77	2.81E-101	4.41E-97
nmSC Up	RASSF4	0.67	0.13	1.40	2.84E-100	4.45E-96
nmSC Down	DYNLT1	0.83	0.98	-0.70	7.57E-134	1.19E-129
nmSC Down	EDNRB	0.95	1.00	-0.73	4.98E-131	7.82E-127
nmSC Down	ID2	0.89	0.98	-0.82	1.31E-102	2.05E-98
nmSC Down	DYNLT1	0.81	0.96	-0.66	5.92E-102	9.29E-98
nmSC Down	DYNLT1	0.85	0.97	-0.61	5.11E-94	8.03E-90
nmSC Down	POSTN	0.60	0.85	-0.99	2.58E-72	4.06E-68
nmSC Down	HNRNPA1	0.69	0.95	-0.73	5.28E-69	8.29E-65
nmSC Down	RBM3	0.71	0.91	-0.67	5.24E-66	8.23E-62
nmSC Down	ERH	0.78	0.95	-0.60	1.05E-65	1.65E-61
nmSC Down	SERPINE 2	0.78	0.88	-0.90	9.23E-61	1.45E-56

Table 10. Markers genes for SNAT scRNAseq dataset clusters.

Gene	Cluster	Proportion	Proportion	Log_2FC	P	FDR

		cluster > 0	other clusters >0			
NCMAP	mSC cluster 2	0.99	0.51	1.36	5.56E-157	8.74E-153
SLC36A2	mSC cluster 2	0.92	0.38	1.26	1.29E-128	2.03E-124
FAM178B	mSC cluster 2	0.79	0.28	1.31	4.81E-113	7.55E-109
ECSCR	mSC cluster 1	0.85	0.19	1.45	1.77E-149	2.77E-145
PMP2	mSC cluster 1	0.93	0.34	1.70	1.34E-143	2.10E-139
FABP9	mSC cluster 1	0.92	0.33	1.69	1.64E-143	2.57E-139
MFAP5	mSC cluster 3	1.00	0.10	2.48	2.20E-158	3.46E-154
APOD	mSC cluster 3	0.99	0.12	2.29	2.43E-136	3.81E-132
SPP1	mSC cluster 3	0.89	0.10	2.26	3.41E-124	5.36E-120
C4A	nm(R)SC	0.69	0.09	1.70	3.53E-206	5.54E-202
ALDH1A1	nm(R)SC	0.65	0.08	1.70	2.20E-200	3.45E-196
F3	nm(R)SC	0.65	0.09	1.66	1.17E-182	1.83E-178
CDCA3	prol. SC	0.88	0.08	2.13	9.87E-245	1.55E-240
BIRC5	prol. SC	0.97	0.14	2.29	3.99E-223	6.27E-219
CDK1	prol. SC	0.87	0.16	2.17	3.47E-165	5.44E-161
POSTN	iSC	0.85	0.51	1.04	3.10E-116	4.87E-112
SMIM5	iSC	0.48	0.24	0.94	1.02E-47	1.60E-43
CCND2	iSC	0.58	0.36	0.89	7.06E-45	1.11E-40
CDKN1C	pmSC	0.96	0.51	1.46	7.81E-113	1.23E-108
CSRP2	pmSC	0.99	0.59	1.02	2.91E-77	4.58E-73
LPCAT1	pmSC	0.92	0.55	1.00	2.10E-74	3.30E-70
ENTPD2	tSC	0.97	0.53	1.19	5.28E-125	8.29E-121
CLDN11	tSC	0.66	0.14	1.14	8.61E-117	1.35E-112
ID3	tSC	0.77	0.31	1.20	2.69E-83	4.22E-79

509

FIGURES

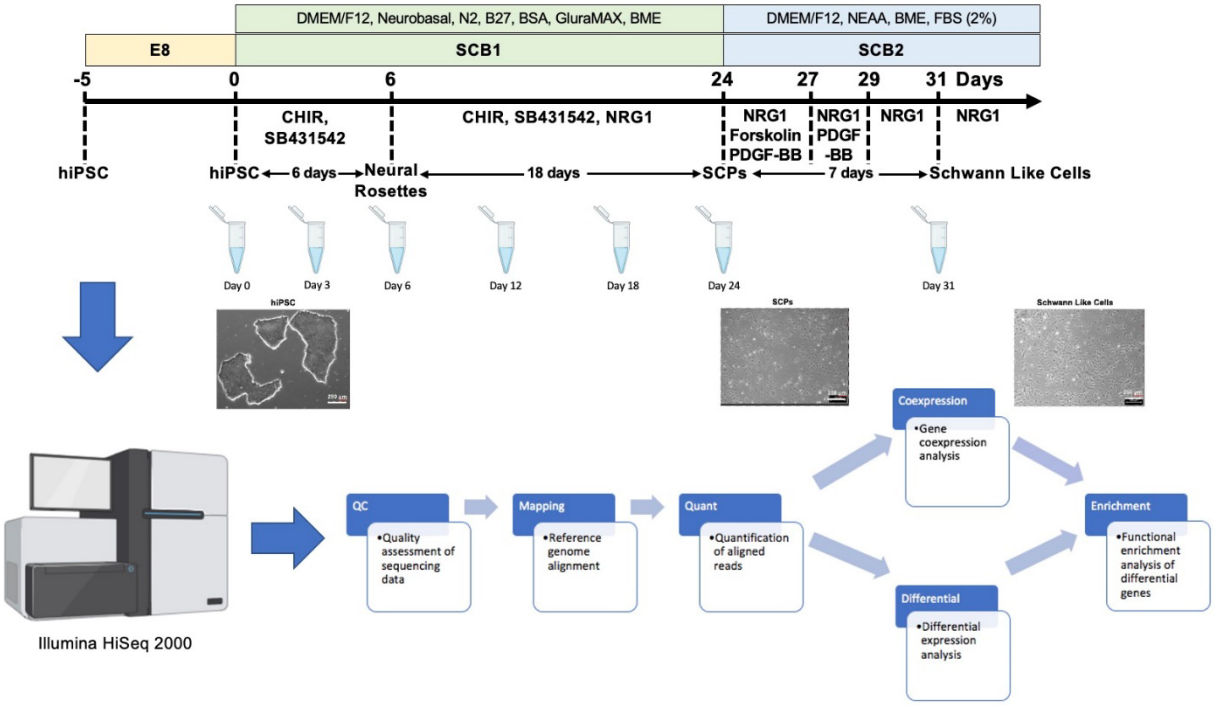

Fig 1. Workflow of directed differentiation of hiPSCs into human Schwan like cells including different stages where samples were collected for sequencing analysis. Schematic representation of the differentiation of hiPSCs into Schwann cell precursors (SCPs) and Schwann like cells (SLCs) (Upper panel). Representative bright-field images showing the process of differentiation into SCPs and SLCs. Scale bar, 100 mm (middle panel). Steps involve sequencing and data analysis (lower panel).

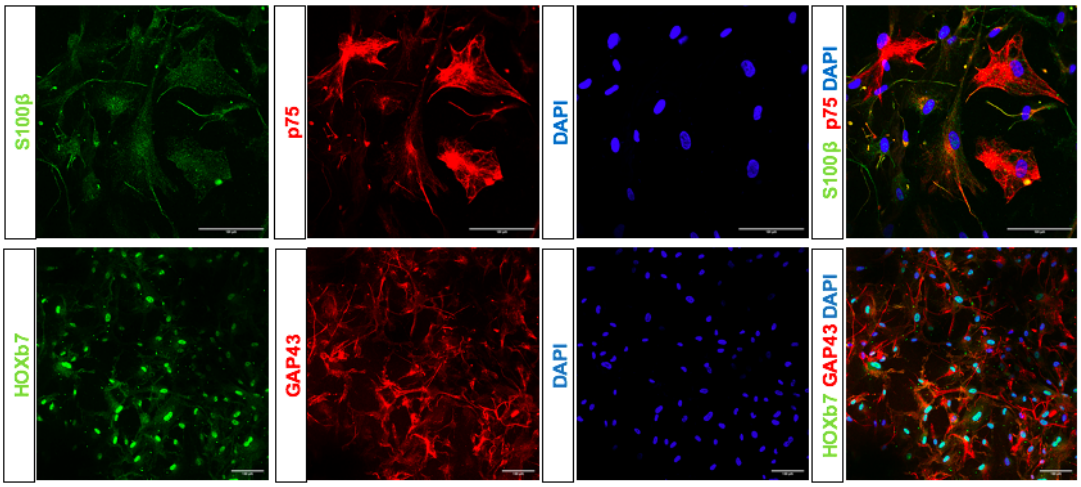

Fig. 2 Characterization of hiPSC derived Schwan like cells. Schwann cell differentiation was confirmed by positive immunocytochemical staining for **(A)** S100β (green), p75 (red) in upper panel and **(B)** HOXb7 (green), GAP43 (red) in lower panel after 31 days of differentiation. DAPI (blue) was used to stain the cell nuclei. Scale bars, 100 mm.

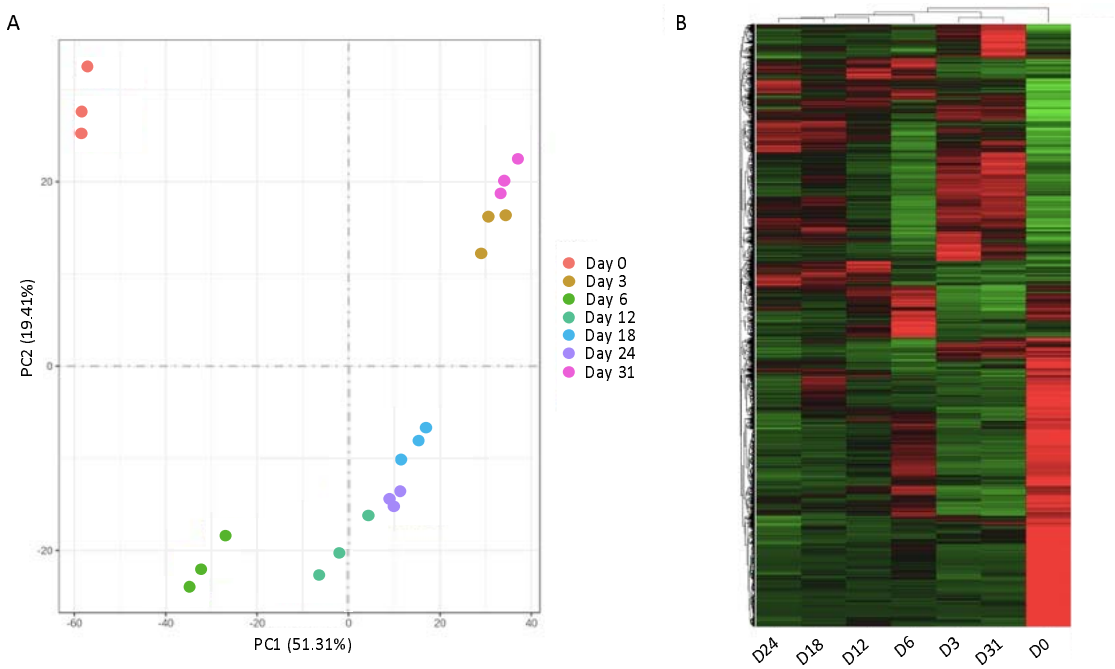

Fig. 3 Differential gene expression analysis of iPSC differentiation to SLCs. **A)** Timepoints representing stages of differentiation cluster discretely by PCA. **B)** Heatmap of differentially expressed genes across different timepoints where the rows (genes) were clustered using hierarchical clustering.

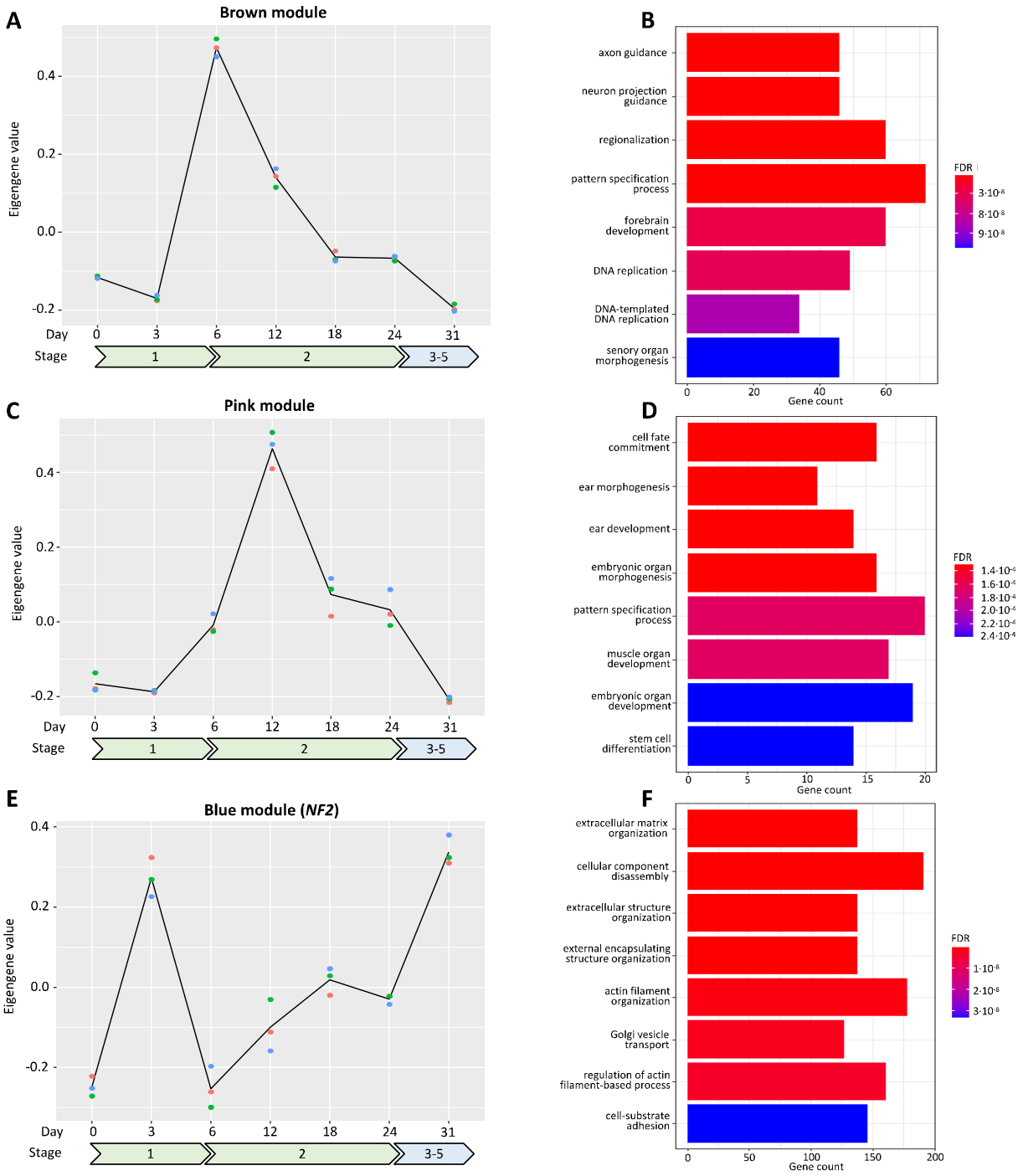

to tissue structure and neural development. **(A)** Brown module eigengene changes over the study timepoints. **(B)** Significant ontology terms from functional enrichment analysis for brown module. **(C)** Pink module eigengene changes over the study timepoints. **(D)** Significant ontology

terms from functional enrichment analysis for the pink module. **E)** Blue module (containing *NF2*) eigengene changes over the study timepoints. **F)** Significant ontology terms from functional enrichment analysis for the blue module.

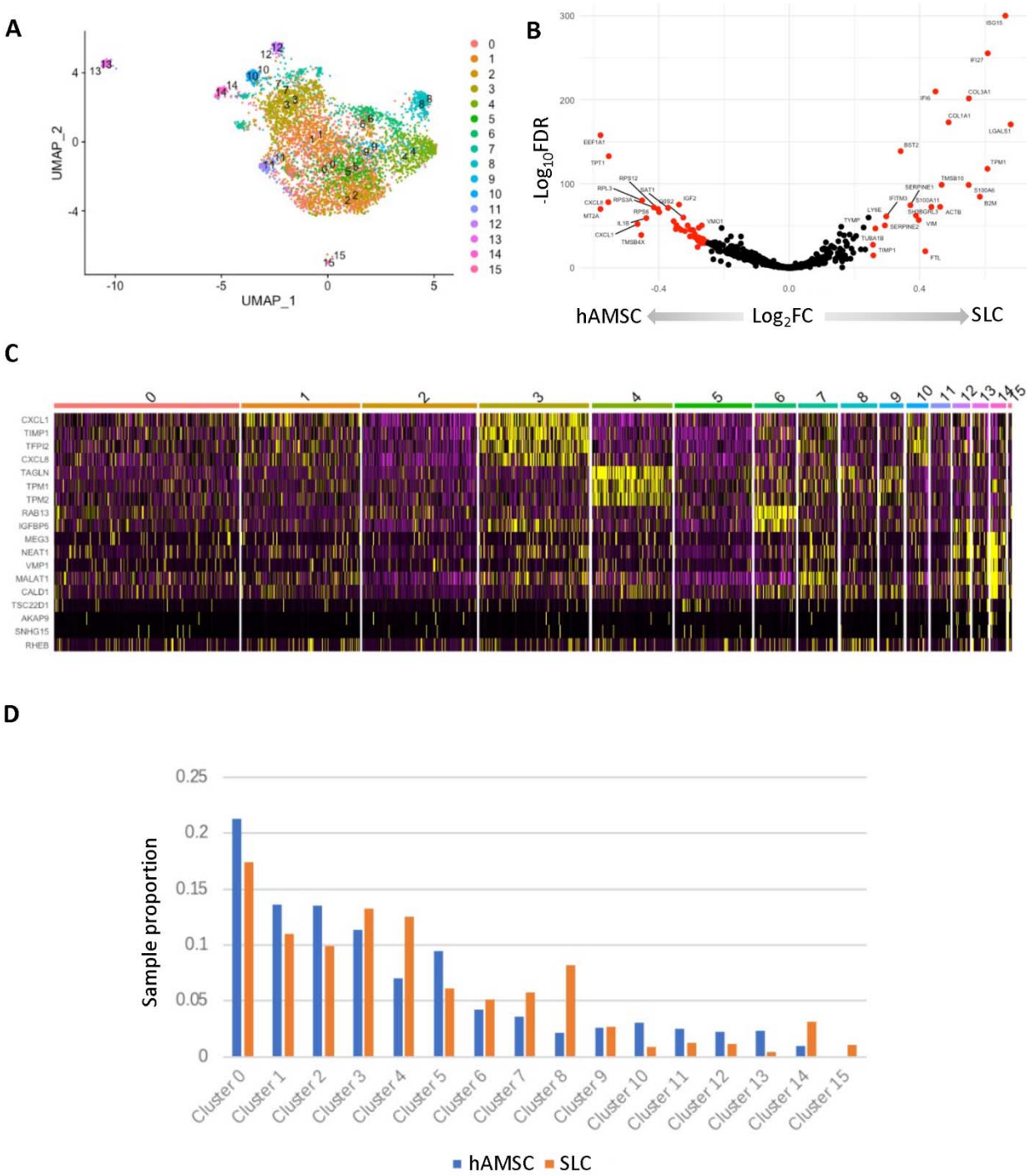

Fig. 5 SLC-SUMC scRNA-seq analysis. **(A)** Scatter plot of 16 clusters identified from the integrated dataset of GSE161066. **(B)** Volcano plot of differential expression genes when compared between hAMSCs and SLCs. **(C)** Heatmap of cluster specific markers. **(D)** Proportion of the clusters in both hAMSCs and SLCs from the integrated dataset of GSE161066.

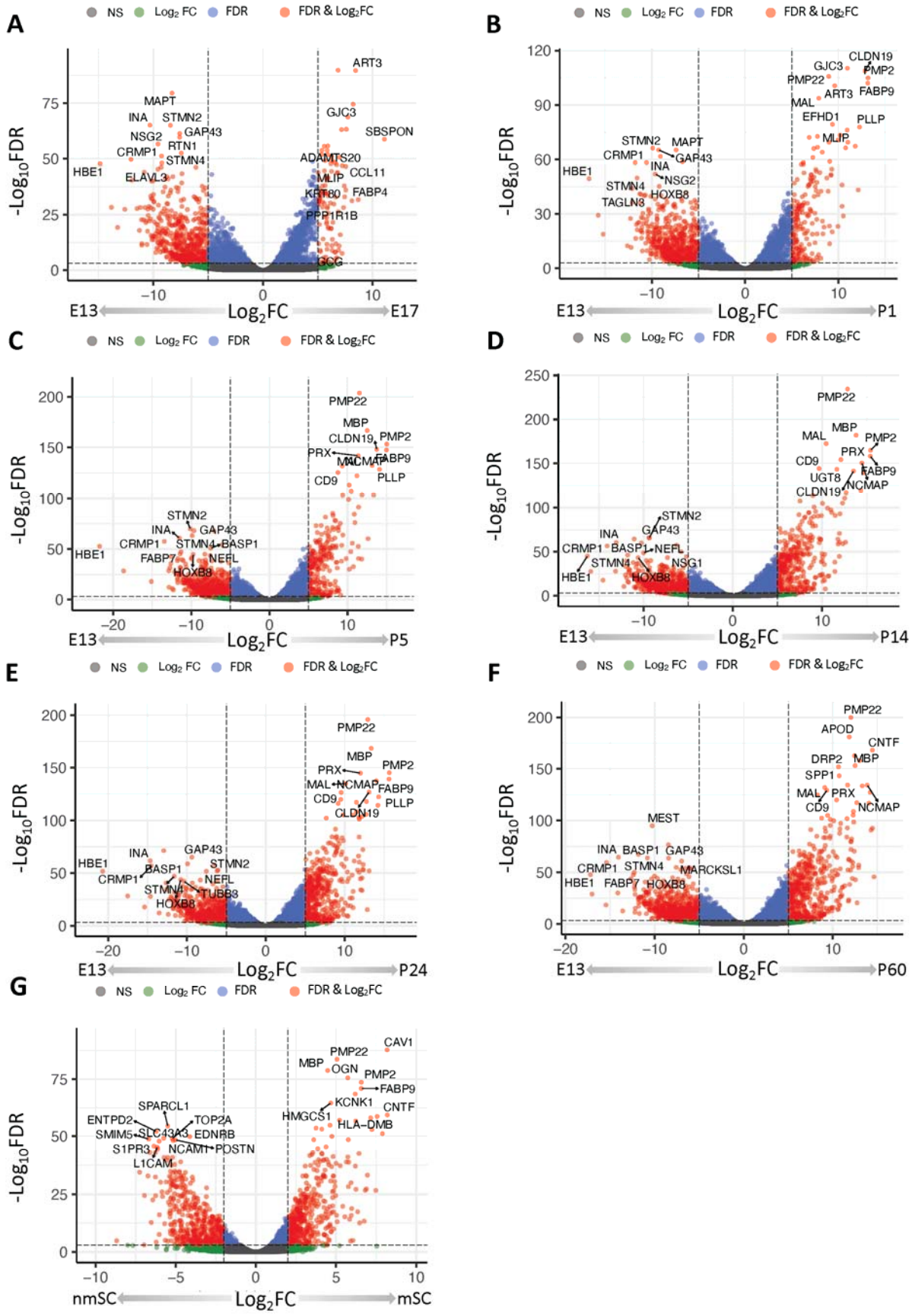
A
NS Log2 FC FDR FDR & Log2FC
-Log10FDR
Log2FC
E13
E17
ART3
MAPT
INA
STMN2
GAP43
NSG2
RTN1
CRMP1
STMN4
HBE1
ELAVL3
GJC3
SBSPON
ADAMTS20
MLIP
CCL11
KRT80
FABP4
PPP1R1B
GCG
B
NS Log2 FC FDR FDR & Log2FC
-Log10FDR
Log2FC
E13
P1
CLDN19
GJC3
PMP2
PMP22
ART3
FABP9
MAL
EFHD1
PLLP
MLIP
STMN2
MAPT
CRMP1
GAP43
INA
NSG2
HBE1
STMN4
HOXB8
TAGLN3
C
NS Log2 FC FDR FDR & Log2FC
-Log10FDR
Log2FC
E13
P5
PMP22
MBP
CLDN19
PMP2
PRX
NCMAP
FABP9
CD9
PLLP
STMN2
INA
GAP43
CRMP1
STMN4
BASP1
HBE1
FABP7
NEFL
HOXB8
D
NS Log2 FC FDR FDR & Log2FC
-Log10FDR
Log2FC
E13
P14
PMP22
MAL
MBP
PMP2
PRX
CD9
FABP9
UGT8
NCMAP
CLDN19
STMN2
INA
GAP43
CRMP1
BASP1
NEFL
STMN4
NSG1
HBE1
HOXB8
E
NS Log2 FC FDR FDR & Log2FC
-Log10FDR
Log2FC
E13
P24
PMP22
MBP
PRX
PMP2
MAL
NCMAP
FABP9
CD9
PLLP
CLDN19
INA
GAP43
HBE1
BASP1
STMN2
CRMP1
NEFL
STMN4
TUBB3
HOXB8
F
NS Log2 FC FDR FDR & Log2FC
-Log10FDR
Log2FC
E13
P60
PMP22
APOD
CNTF
DRP2
MBP
SPP1
MAL
PRX
CD9
NCMAP
MEST
INA
BASP1
GAP43
CRMP1
STMN4
MARCKSL1
HBE1
FABP7
HOXB8
G
NS Log2 FC FDR FDR & Log2FC
-Log10FDR
Log2FC
nmSC
mSC
CAV1
PMP22
MBP
OGN
PMP2
FABP9
KCNK1
CNTF
HMGCS1
HLA-DMB
SPARCL1
ENTPD2
TOP2A
SMIM5
SLC43A3
EDNRB
S1PR3
NCAM1
POSTN
L1CAM

546

Fig. 6 SNAT RNA-seq analysis. DGE results are shown in volcano plots for E17 **(A)**, P1 **(B)**, P5 **(C)**, P14 **(D)**, P24 **(E),** and P60 **(F)** as compared to E13 and myelinating vs. non-myelinating Schwann cells **(G)**.

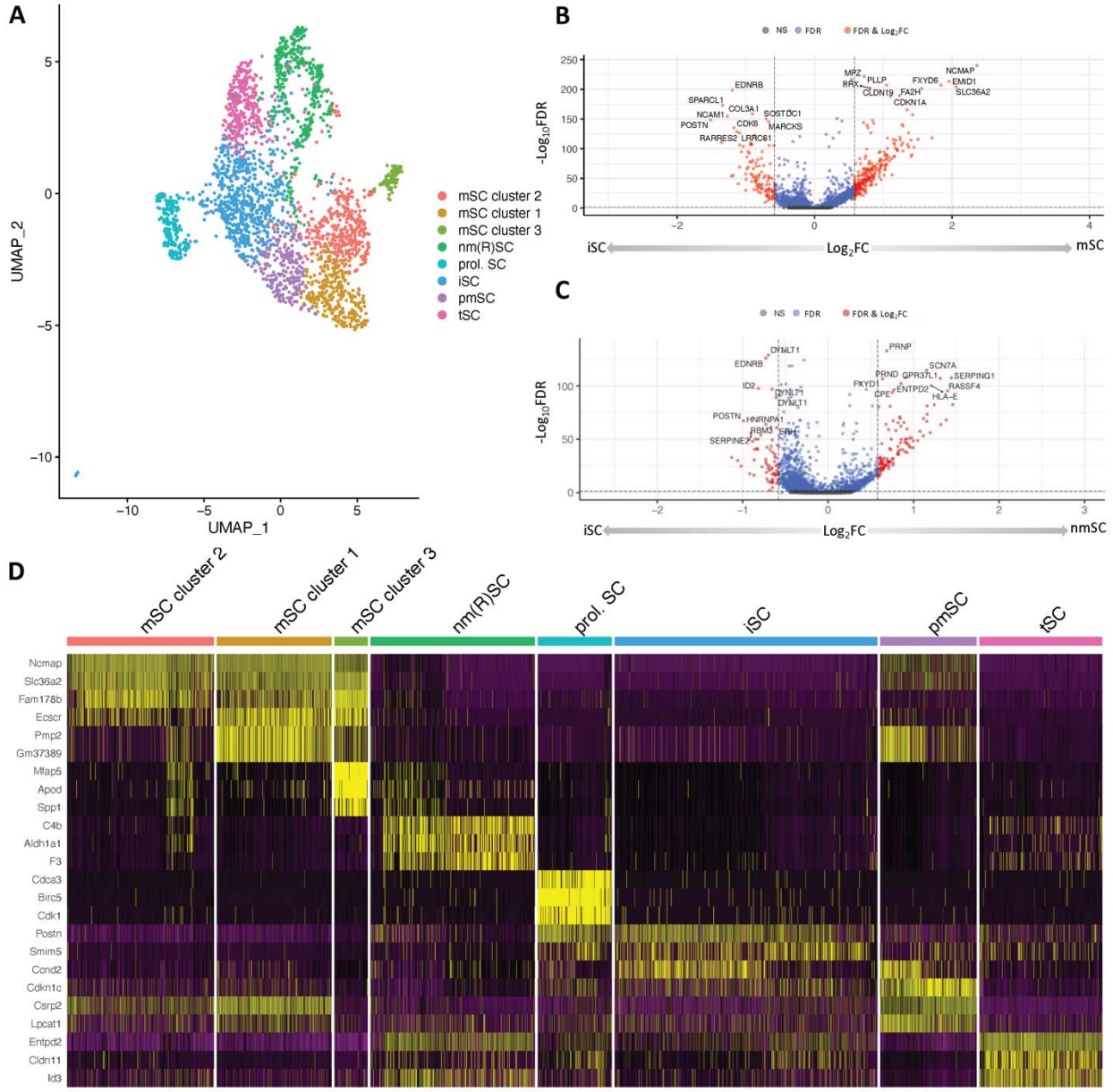

Fig. 7 SNAT scRNA-seq analysis. **(A)** Scatterplot of 8 clusters identified from the SNAT study representing different stages of Schwann cell development and myelination. **(B)** DGE analysis comparing mSC vs iSC. **(C)** DGE results comparing nmSC vs iSC. **(D)** Heatmap of cluster specific markers (top 3).

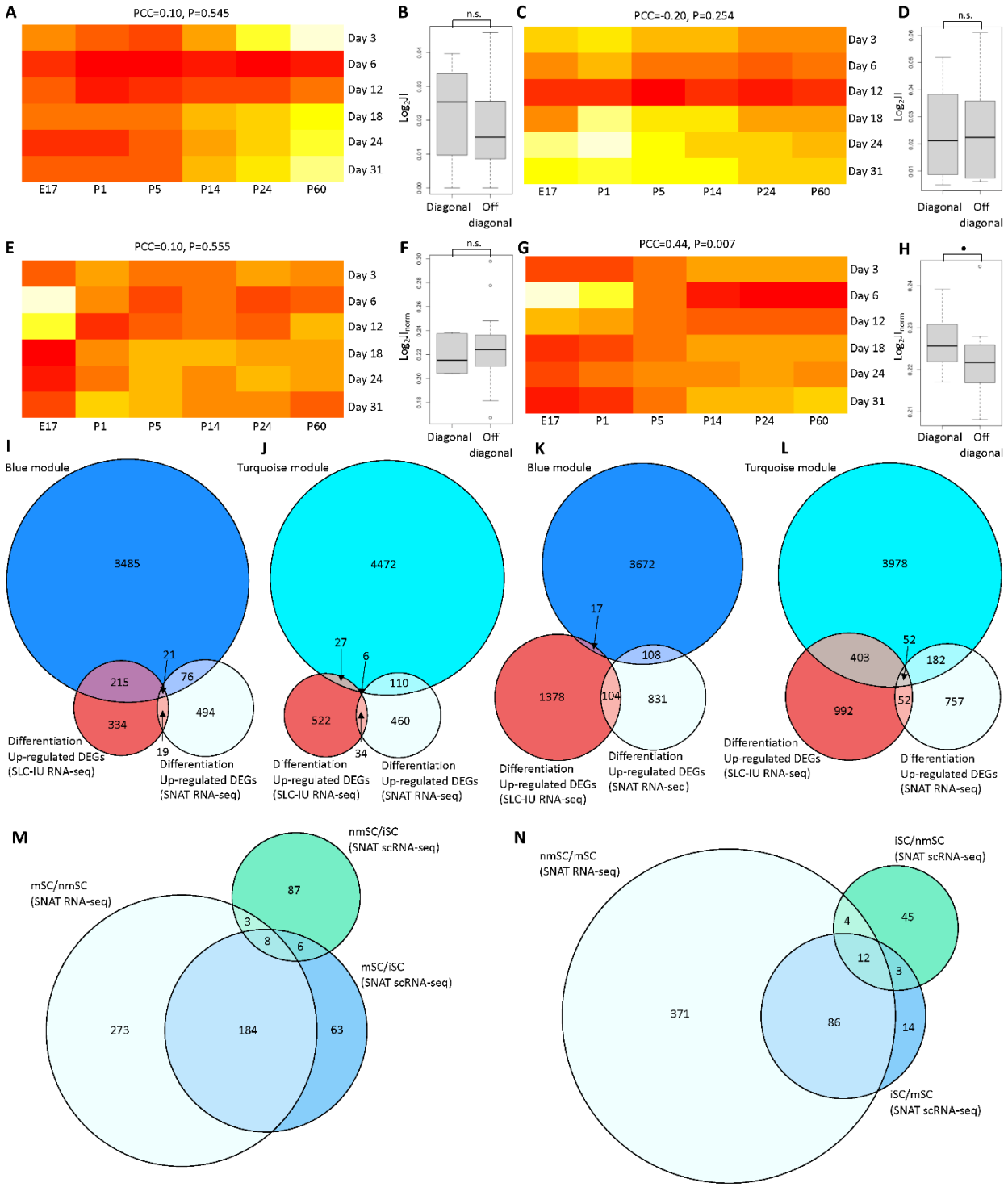

Fig. 8 Comparison of identified gene lists. **(A)** JI matrix of SLC-IU differentiation up-regulated DEGs versus SNAT up-regulated DEGs with comparison of JI matrix diagonal to non-diagonal

(B). **(C)** JI matrix of SLC-IU differentiation down-regulated DEGs versus SNAT down-regulated DEGs with comparison of JI matrix diagonal to non-diagonal **(D)**. **(E)** Normalized JI matrix of averaged SLC-IU differentiation up/down-regulated DEGs and SNAT up/down-regulated DEGs with comparison of JI matrix diagonal to non-diagonal **(F). (G)** Normalized JI matrix of averaged SLC-IU differentiation up/down-regulated DEGs (|log2FC| > 0.58 and an FDR < 0.05) and SNAT up/down-regulated DEGs (|log2FC| > 0.58 and an FDR < 0.05) with comparison of JI matrix diagonal to non-diagonal **(F)**. Comparison of SLC-IU differentiation up-regulated DEGs within the blue module **(I)** and turquoise module **(J)** versus SNAT up-regulated DEGs. **(K)** Comparison SLC-IU differentiation down-regulated DEGs within the blue module **(K)** and turquoise module **(L)** versus SNAT down-regulated DEGs. (**M)** Comparison of mSC vs. iSC markers and nmSC vs. iSC markers from SNAT scRNA-seq and mSC up-regulated DEGs from SNAT RNA-seq. **(N)** Comparison of iSC vs. mSC markers and iSC vs. nmSC markers from SNAT scRNA-seq and mSC down-regulated DEGs from SNAT RNA-seq.

REFERENCES

1. Fallon, M. and P. Tadi, *Histology, Schwann Cells*, in *StatPearls*. 2023: Treasure Island (FL).
2. Salzer, J.L. and B. Zalc, *Myelination.* Curr Biol, 2016. **26**(20): p. R971-R975.
3. Goncalves, N.P., et al., *Schwann cell interactions with axons and microvessels in diabetic neuropathy.* Nat Rev Neurol, 2017. **13**(3): p. 135-147.
4. Sheikh, M.M. and O. De Jesus, *Vestibular Schwannoma*, in *StatPearls*. 2023: Treasure Island (FL).
5. Carlson, M.L. and M.J. Link, *Vestibular Schwannomas.* N Engl J Med, 2021. **384**(14): p. 1335-1348.
6. Evans, D.G., *Neurofibromatosis type 2 (NF2): a clinical and molecular review.* Orphanet J Rare Dis, 2009. **4**: p. 16.
7. Rouleau, G.A., et al., *Alteration in a new gene encoding a putative membrane-organizing protein causes neuro-fibromatosis type 2.* Nature, 1993. **363**(6429): p. 515-21.
8. Evans, D.G., et al., *A clinical study of type 2 neurofibromatosis.* Q J Med, 1992. **84**(304): p. 603-18.
9. Agnihotri, S., et al., *The genomic landscape of schwannoma.* Nat Genet, 2016. **48**(11): p. 1339-1348.
10. Leventoux, N., et al., *Human Astrocytes Model Derived from Induced Pluripotent Stem Cells.* Cells, 2020. **9**(12).
11. Perriot, S., et al., *Differentiation of functional astrocytes from human-induced pluripotent stem cells in chemically defined media.* STAR Protoc, 2021. **2**(4): p. 100902.
12. Perriot, S., et al., *Human Induced Pluripotent Stem Cell-Derived Astrocytes Are Differentially Activated by Multiple Sclerosis-Associated Cytokines.* Stem Cell Reports, 2018. **11**(5): p. 1199-1210.
13. Voulgaris, D., P. Nikolakopoulou, and A. Herland, *Generation of Human iPSC-Derived Astrocytes with a mature star-shaped phenotype for CNS modeling.* Stem Cell Rev Rep, 2022. **18**(7): p. 2494-2512.
14. Abud, E.M., et al., *iPSC-Derived Human Microglia-like Cells to Study Neurological Diseases.* Neuron, 2017. **94**(2): p. 278-293 e9.
15. Hasselmann, J. and M. Blurton-Jones, *Human iPSC-derived microglia: A growing toolset to study the brain's innate immune cells.* Glia, 2020. **68**(4): p. 721-739.
16. McQuade, A., et al., *Development and validation of a simplified method to generate human microglia from pluripotent stem cells.* Mol Neurodegener, 2018. **13**(1): p. 67.
17. Autar, K., et al., *A functional hiPSC-cortical neuron differentiation and maturation model and its application to neurological disorders.* Stem Cell Reports, 2022. **17**(1): p. 96-109.
18. Vierbuchen, T., et al., *Direct conversion of fibroblasts to functional neurons by defined factors.* Nature, 2010. **463**(7284): p. 1035-41.
19. Brennand, K.J., et al., *Modelling schizophrenia using human induced pluripotent stem cells.* Nature, 2011. **473**(7346): p. 221-5.
20. Page, S.C., et al., *Electrophysiological measures from human iPSC-derived neurons are associated with schizophrenia clinical status and predict individual cognitive performance.* Proc Natl Acad Sci U S A, 2022. **119**(3).
21. Park, I.H., et al., *Disease-specific induced pluripotent stem cells.* Cell, 2008. **134**(5): p. 877-86.
22. Penney, J., W.T. Ralvenius, and L.H. Tsai, *Modeling Alzheimer's disease with iPSC-derived brain cells.* Mol Psychiatry, 2020. **25**(1): p. 148-167.
23. Krieger, T.G., et al., *Modeling glioblastoma invasion using human brain organoids and single-cell transcriptomics.* Neuro Oncol, 2020. **22**(8): p. 1138-1149.

24. Sancho-Martinez, I., et al., *Establishment of human iPSC-based models for the study and targeting of glioma initiating cells.* Nat Commun, 2016. **7**: p. 10743.
25. Schloo, C. and L.M. Kutscher, *Modeling brain and neural crest neoplasms with human pluripotent stem cells.* Neuro Oncol, 2023. **25**(7): p. 1225-1235.
26. Zhang, S., et al., *Development of human induced pluripotent stem cell (iPSC) line from a 60year old female patient with multiple schwannoma.* Stem Cell Res, 2017. **19**: p. 31-33.
27. Langfelder, P. and S. Horvath, *WGCNA: an R package for weighted correlation network analysis.* BMC Bioinformatics, 2008. **9**: p. 559.
28. Garcia-Moreno, A., et al., *Functional Enrichment Analysis of Regulatory Elements.* Biomedicines, 2022. **10**(3).
29. Wei, Z., et al., *A Subpopulation of Schwann Cell-Like Cells With Nerve Regeneration Signatures Is Identified Through Single-Cell RNA Sequencing.* Front Physiol, 2021. **12**: p. 637924.
30. Gerber, D., et al., *Transcriptional profiling of mouse peripheral nerves to the single-cell level to build a sciatic nerve ATlas (SNAT).* Elife, 2021. **10**.
31. Kim, H.S., et al., *Schwann Cell Precursors from Human Pluripotent Stem Cells as a Potential Therapeutic Target for Myelin Repair.* Stem Cell Reports, 2017. **8**(6): p. 1714-1726.
32. Liu, Z., et al., *Specific marker expression and cell state of Schwann cells during culture in vitro.* PLoS One, 2015. **10**(4): p. e0123278.
33. Chen, J., et al., *ToppGene Suite for gene list enrichment analysis and candidate gene prioritization.* Nucleic Acids Res, 2009. **37**(Web Server issue): p. W305-11.
34. Hao, Y., et al., *Integrated analysis of multimodal single-cell data.* Cell, 2021. **184**(13): p. 3573-3587 e29.
35. Choudhary, S. and R. Satija, *Comparison and evaluation of statistical error models for scRNA-seq.* Genome Biol, 2022. **23**(1): p. 27.
36. Lause, J., P. Berens, and D. Kobak, *Analytic Pearson residuals for normalization of single-cell RNA-seq UMI data.* Genome Biol, 2021. **22**(1): p. 258.
37. Korsunsky, I., et al., *Fast, sensitive and accurate integration of single-cell data with Harmony.* Nat Methods, 2019. **16**(12): p. 1289-1296.
38. Tran, H.T.N., et al., *A benchmark of batch-effect correction methods for single-cell RNA sequencing data.* Genome Biol, 2020. **21**(1): p. 12.
39. McInnes, L., J. Healy, and J. Melville, *Umap: Uniform manifold approximation and projection for dimension reduction.* arXiv preprint arXiv:1802.03426, 2018.
40. Wang, J., et al., *Clinical and tumor significance of tropomyosin-1 expression levels in renal cell carcinoma.* Oncol Rep, 2015. **33**(3): p. 1326-34.
41. Wang, J., et al., *Tropomyosin-1 Functions as a Tumor Suppressor with Respect to Cell Proliferation, Angiogenesis and Metastasis in Renal Cell Carcinoma.* J Cancer, 2019. **10**(10): p. 2220-2228.
42. Deng, B., *Mouse models and induced pluripotent stem cells in researching psychiatric disorders.* Stem Cell Investig, 2017. **4**: p. 62.
43. Bashour, A.M., et al., *The neurofibromatosis type 2 gene product, merlin, reverses the F-actin cytoskeletal defects in primary human Schwannoma cells.* Mol Cell Biol, 2002. **22**(4): p. 1150-7.
44. Hennigan, R.F., et al., *The NF2 tumor suppressor regulates microtubule-based vesicle trafficking via a novel Rac, MLK and p38(SAPK) pathway.* Oncogene, 2013. **32**(9): p. 1135-43.
45. Kruglov, O., et al., *Melanoma-associated repair-like Schwann cells suppress anti-tumor T-cells via 12/15-LOX/COX2-associated eicosanoid production.* Oncoimmunology, 2023. **12**(1): p. 2192098.
46. Chen, X., X. Yu, and E. Shen, *Overexpression of CDKN2B is involved in poor gastric cancer prognosis.* J Cell Biochem, 2019. **120**(12): p. 19825-19831.

47. Tu, Q., et al., *CDKN2B deletion is essential for pancreatic cancer development instead of unmeaningful co-deletion due to juxtaposition to CDKN2A.* Oncogene, 2018. **37**(1): p. 128-138.
48. Wrensch, M., et al., *Variants in the CDKN2B and RTEL1 regions are associated with high-grade glioma susceptibility.* Nat Genet, 2009. **41**(8): p. 905-8.
49. Xia, W., et al., *ANXA1 directs Schwann cells proliferation and migration to accelerate nerve regeneration through the FPR2/AMPK pathway.* FASEB J, 2020. **34**(10): p. 13993-14005.